ResearchGate

See discussions, stats, and author profiles for this publication at: https://www.researchgate.net/publication/14142858

Crystal structure of the hydroxylase component of methane monooxygenase from Methylosinus trichosporium OB3b. Protein Sci 6:556–568

ARTICLE *in* PROTEIN SCIENCE · MARCH 2008

Impact Factor: 2.85 · DOI: 10.1002/pro.5560060305 · Source: PubMed

CITATIONS
132

READS
30

7 AUTHORS, INCLUDING:

Bradley J Wallar
Grand Valley State University
25 PUBLICATIONS **2,290** CITATIONS

SEE PROFILE

Doug H Ohlendorf
University of Minnesota Twin Cities
79 PUBLICATIONS **5,448** CITATIONS

SEE PROFILE

Available from: Doug H Ohlendorf
Retrieved on: 24 January 2016

Protein Science (1997), 6:556–568. Cambridge University Press. Printed in the USA.
Copyright © 1997 The Protein Society

97/108R
(submitted as a reprint)

Crystal structure of the hydroxylase component of methane monooxygenase from *Methylosinus trichosporium* OB3b

NATESAN ELANGO, RAMASWAMY RADHAKRISHNAN[1], WAYNE A. FROLAND[2], BRADLEY J. WALLAR, CATHLEEN A. EARHART, JOHN D. LIPSCOMB, AND DOUGLAS H. OHLENDORF

Department of Biochemistry, Medical School, University of Minnesota, Minneapolis, Minnesota 55455

(RECEIVED October 3, 1996; ACCEPTED December 11, 1996)

Abstract

Methane monooxygenase (MMO), found in aerobic methanotrophic bacteria, catalyzes the O_2-dependent conversion of methane to methanol. The soluble form of the enzyme (sMMO) consists of three components: a reductase, a regulatory "B" component (MMOB), and a hydroxylase component (MMOH), which contains a hydroxo-bridged dinuclear iron cluster. Two genera of methanotrophs, termed Type X and Type II, which differ markedly in cellular and metabolic characteristics, are known to produce the sMMO. The structure of MMOH from the Type X methanotroph *Methylococcus capsulatus* Bath (MMO Bath) has been reported recently. Two different structures were found for the essential diiron cluster, depending upon the temperature at which the diffraction data were collected. In order to extend the structural studies to the Type II methanotrophs and to determine whether one of the two known MMOH structures is generally applicable to the MMOH family, we have determined the crystal structure of the MMOH from Type II *Methylosinus trichosporium* OB3b (MMO OB3b) in two crystal forms to 2.0 Å and 2.7 Å resolution, respectively, both determined at 18 °C. The crystal forms differ in that MMOB was present during crystallization of the second form. Both crystal forms, however, yielded very similar results for the structure of the MMOH. Most of the major structural features of the MMOH Bath were also maintained with high fidelity. The two irons of the active site cluster of MMOH OB3b are bridged by two OH (or one OH and one H_2O), as well as both carboxylate oxygens of Glu α144. This bis-μ-hydroxo-bridged "diamond core" structure, with a short Fe-Fe distance of 2.99 Å, is unique for the resting state of proteins containing analogous diiron clusters, and is very similar to the structure reported for the cluster from flash frozen (−160 °C) crystals of MMOH Bath, suggesting a common active site structure for the soluble MMOHs. The high-resolution structure of MMOH OB3b indicates 26 consecutive amino acid sequence differences in the β chain when compared to the previously reported sequence inferred from the cloned gene. Fifteen additional sequence differences distributed randomly over the three chains were also observed, including Dα209E, a ligand of one of the irons.

Keywords: dinuclear iron cluster; methane oxidation; methanotroph; oxygen activation; X-ray crystallography

Methanotrophic bacteria utilize methane produced from the metabolism of anaerobic bacteria and other natural sources to satisfy their total carbon and energy requirements (Dalton, 1980; Anthony, 1982). The first and most difficult step of the methane oxidation pathway, in which the stable C-H bond of methane is broken and an oxygen atom inserted to form methanol, is catalyzed by the enzyme methane monooxygenase (MMO) (Dalton, 1980; Feig & Lippard, 1994; Lipscomb, 1994; Wallar & Lipscomb, 1996):

$$CH_4 + O_2 + NAD(P)H + H^+ \rightarrow CH_3OH + H_2O + NAD(P)^+.$$

MMO also catalyzes the adventitious oxidation of a large number of other hydrocarbons up to about C_8 in size (Colby et al., 1977; Dalton, 1980; Higgins et al., 1980; Green & Dalton, 1989; Tsien et al., 1989; Fox et al., 1990b; Andersson et al., 1991; Rataj et al., 1991). MMO exists in both a soluble (sMMO) and a particulate (pMMO) form (Dalton, 1980; Anthony, 1982). sMMO has been purified and characterized from the Type X methanotroph, *Methylococcus capsulatus* Bath (MMO Bath) (Dalton, 1980, 1991; Woodland & Dalton, 1984; Pilkington & Dalton, 1990), and several Type II methanotrophs including, *Methylosinus trichosporium* OB3b

Reprint requests to: Douglas H. Ohlendorf, Department of Biochemistry, Medical School, University of Minnesota, Minneapolis, Minnesota 55455; e-mail: ohlen@dccc.med.umn.edu.

[1]Present address: Center for Macromolecular Crystallography, University of Alabama at Birmingham, Birmingham, Alabama 35294.

[2]Present address: Department of Chemistry, University of California at Berkeley, Berkeley, California 94720.

(MMO OB3b) (Fox et al., 1989, 1990a), and *Methylobacterium* sp. CRL-26 (Patel & Savas, 1987). The Type X and Type II methanotrophs differ dramatically in cellular morphology, many metabolic pathways, and response to environmental stress (Anthony, 1982), but their MMOs and other methane oxidation pathway enzymes appear to be very similar.

The MMO operons from *M. trichosporium* OB3b and *M. capsulatus* Bath have been cloned and sequenced (Stainthorpe et al., 1989, 1990; Cardy et al., 1991a, 1991b). These studies and direct protein isolation and characterization have shown that MMO is composed of three protein components, each of which is required for efficient substrate hydroxylation coupled to NADH oxidation: a 245-kDa hydroxylase (MMOH), a 40-kDa reductase (MMOR), and a 15-kDa protein called component B (MMOB). The hydroxylase has a dimeric protomer structure, with each protomer containing three subunits (α,β,γ) (Rosenzweig et al., 1993; Froland et al., 1994) and a hydroxo-bridged dinuclear iron cluster (Fox et al., 1988, 1993; DeWitt et al., 1991; DeRose et al., 1993; Thomann et al., 1993). MMOH and its diiron clusters are essential for catalysis by MMO (Fox et al., 1989). The cluster is contained in the α subunit adjacent to an internal hydrophobic pocket that forms the active site (Rosenzweig et al., 1993). The genetic studies indicate a 66% sequence identity between the hydroxylase subunits of the two species that have been cloned and sequenced (Stainthorpe et al., 1989, 1990; Cardy et al., 1991a, 1991b).

The other two components of MMO also serve important functions. In addition to transferring electrons to MMOH, MMOR forms a specific complex with the β subunit of MMOH (Fox et al., 1991), which has the effect of adjusting the relative redox potentials of the two cluster irons so that two-electron transfer is favored (Paulsen et al., 1994; Y. Liu, J. Nesheim, K.E. Paulsen, M.T. Stankovich, & J.D. Lipscomb, manuscript submitted). Component B has been shown to bind specifically to the α subunit of MMOH (Fox et al., 1991). This complex has profound effects on the rate of certain reactions in the catalytic cycle, the redox potential of the diiron cluster, the structure of MMOH, and the product distribution and yield of the overall reaction (Fox et al., 1991; Froland et al., 1992; Liu et al., 1995b, 1995c).

All steps of the catalytic cycle of sMMO appear to involve the diiron cluster (Fig. 1) (Fox et al., 1989; Lee et al., 1993b). The first step in the catalytic cycle is the reduction of the diiron cluster to the diferrous state (Fox et al., 1989). Next, O_2 binds to the cluster in two steps, forming a peroxo species termed compound P (Lee et al., 1993b; Liu et al., 1994, 1995a, 1995c). This species then converts spontaneously to a high valent iron-oxo species (compound Q) (Lee et al., 1993a, 1993b) in which both irons appear to be in the Fe(IV) state. This species is electronically and functionally analogous to the proposed mononuclear Fe(IV) oxenoid π cation radical species (compound I) produced by cytochrome P-450 and horseradish peroxidase during catalysis (Ortiz de Montellano, 1985; McMurry & Groves, 1986). At this stage, the highly oxidized diiron cluster reacts with substrate to form the hydroxylated product and the resting diferric state of MMOH after passing through other intermediates that have been characterized partially (Priestley et al., 1992; Lee et al., 1993b; Nesheim & Lipscomb, 1996).

The crystal structure of the hydroxylase component from the Type X methanotroph *M. capsulatus* Bath has been reported in the oxidized state at 4 °C and −160 °C (Rosenzweig et al., 1993, 1995) as well as the reduced state at −160 °C (Rosenzweig et al., 1995). Interestingly, the structure of the dinuclear iron cluster was found to be different in each of the conditions and redox states. In particular, the two structures of the cluster in the resting diferric enzyme differed significantly in that, at 4 °C, the two irons were bridged by Glu α144, a hydroxide moiety, and an exogenous acetate to give an Fe-Fe distance of 3.4 Å, whereas the structure determined at −160 °C revealed Glu α144, a hydroxide, and a water as bridging ligands to give an Fe-Fe distance of 3.1 Å. The latter structure is consistent with model compounds for the diiron clusters containing a so-called "diamond core" with two bridging oxygen ligands (see, for example, Zang et al., 1994; Que & Dong, 1996), as well as with EXAFS studies of MMOH OB3b that indicated a predominant Fe-Fe distance of about 3 Å (Shu et al., 1996a).

In order to determine whether one of the structures of diferric MMOH Bath is characteristic of MMOHs in general, and to extend structural studies to the Type II methanotrophs, we have determined the X-ray crystal structure of MMOH OB3b. Reported here are the 18 °C structures of MMOH OB3b to 2 Å resolution and of MMOH OB3b crystallized in the presence of MMOB to 2.7 Å resolution. We find that the overall structures of MMOHs from the Type X and Type II methanotrophs are very similar, and that the MMOH OB3b forms contain a diiron cluster with a short Fe-Fe distance [2.99 Å in crystal form 1 (MMOH alone) and 3.07 Å in crystal form 2 (MMOB present during crystallization)] and a diamond core oxygen bridge structure. This suggests that the diamond core structure is a common characteristic of MMOH from these widely divergent methanotrophs and may be an important feature for catalysis.

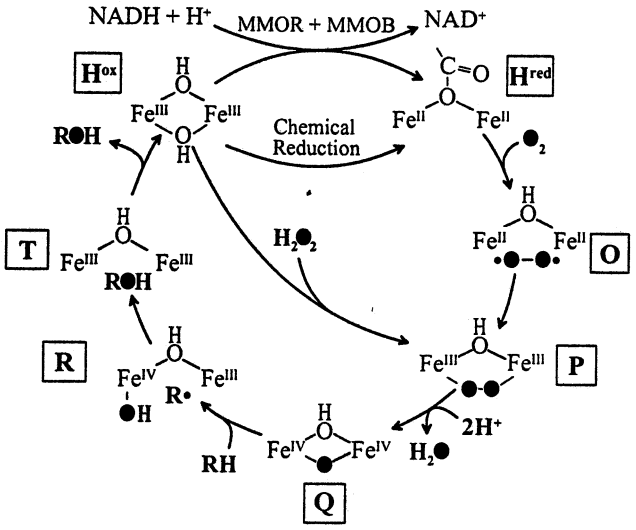

Proposed Catalytic Cycle for MMO

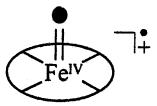

P-450 Activated Species

Fig. 1. Proposed catalytic cycle of methane monooxygenase based on a radical recombination process for substrate hydroxylation. The cytochrome P-450 activated species is the proposed mononuclear Fe(IV) oxenoid π cation radical species equivalent to compound Q. Oxygen atoms derived from O_2 are filled.

Results and discussion

Structure determination

The structure of MMOH OB3b in crystal form 1 was solved by molecular replacement using a monomer of MMOH Bath (Rosenzweig et al., 1993) as the search model and the program XPLOR (Brünger, 1992). Cycles of molecular dynamics refinement and Powell minimization were alternated with map examination, model building, and refinement, to produce the final model that has a crystallographic R-factor of 13.7% for data between 5 and 2 Å, with $F > 2\sigma$ (14.5% with no cut off). This model has 9,334 non-hydrogen atoms from 510 residues in the α chain, 383 residues in the β chain, 167 residues in the γ chain, 731 water molecules, two iron atoms, and two hydroxides. Residues α1–α16, β1–β10, β393–β394, γ1, and γ169 were disordered and not included in the final model. Overall, the electron density map is exceptionally clear, except for the few disordered residues. Figure 2 shows two regions of $2F_o - F_c$ electron density that are typical in quality. Ramachandran plots for the three chains indicate that 93.5% of the residues have (ϕ,ψ) values in the "most favored" region, 6.4% in the "additional allowed" region, and one residue in the "disallowed region" as identified by PROCHECK (Laskowski et al., 1993). Ser γ42 is the only residue in the disallowed region of the Ramachandran plot and is found in an exposed surface loop.

The structure of MMOH OB3b in crystal form 2 was solved using molecular replacement with a refined model of MMOH OB3b in crystal form 1 as a search model. Rigid-body minimization followed by molecular dynamics refinement reduced the R-factor to 19.5% for data between 8 and 2.8 Å, with $F > 2\sigma$. Examination of the electron density maps followed by Powell minimization produced the final model with a crystallographic R-factor of 15.2% for data between 5 and 2 Å, with $F > 2\sigma$ (17.8% with no cut off). This model has 8,605 non-hydrogen atoms from 510 residues in the α chain, 383 residues in the β chain, 167 residues in the γ chain, two water molecules, two iron atoms, and two hydroxides. Ramachandran plots for the three chains indicate that 90.5% of the residues have (ϕ,ψ) values in the "most favored" region, 9.1% in the "additional allowed" region, two residues in the generously allowed region, and one residue in the "disallowed region" as identified by PROCHECK (Laskowski et al., 1993). Again, Ser γ42 is the only residue in the disallowed region of the Ramachandran plot.

A summary of the data collection, refinement, and geometric quality for both of the crystal forms of MMOH OB3b is given in the statistical parameters supplied in Table 1.

Overall structure

The sequence alignment of MMOH OB3b and MMOH Bath with the secondary structural elements labeled to be consistent with that of MMOH Bath is shown in Figure 3. MMOH is almost exclusively helical, with 19 helices in the α chain, 12 helices in the β chain, and 8 helices in the γ chain, accounting for 634 residues of the 1,060 residues in the protomer. There are only three short strands of β structure, accounting for 15 residues.

The three-dimensional structure of MMOH OB3b is shown in Figure 4. The crystallographic twofold, coincident with the crystallographic a axis and relating the two protomers, is vertical in the figure. The heart-shaped dimer is about 130 Å × 90 Å × 70 Å, with the α chains forming the auricles and the β chains forming the ventricles. Although not immediately obvious from the figure, the α and β chains share a similar fold. Two-hundred thirty-three pairs of C_αs can be superimposed with an RMS difference of 2.08 Å. This fold is also found in the R2 protein of ribonucleotide reductase (Nordlund et al., 1990). The interface between the α and β chains is extensive, burying 4,068 Å^2 of the solvent-exposed surface of each chain. Each γ chain is elongated and interacts with the α and β chains away from the symmetry axis.

The active site, which contains the diiron cluster, is located in the α chain between the four long helices, αB (α97–α127), αC (α131–α161), αE (α197–α226), and αF (α231–α257). The distance between the symmetry-related active sites is about 45 Å. A more detailed description of the active site and metal center will be given below.

Several of the helices (α1, αD, αE, αH, βB, βE, βF, and βG) are broken into smaller segments. Most of these distortions occur at one end, sometimes involving 3_{10} or π helical loops. Three of these helices should be noted. Helix αH is interesting in that the central turn of this five-turn helix is a π loop. A basis for this distortion can be seen in the presence of a tryptophan on each turn of this 22-residue helix. These large residues lock side chains to particular locations, leading to this unusual distortion. Helices αE and βE are structurally homologous and are each composed of three shorter helices. The bowing of helix αE is in large part responsible for the formation of the active site cavity in addition to supplying one of the iron ligands (Glu α209).

Structures of form 1 and form 2 of MMOH OB3b are essentially identical. The molecules pack in their respective $C222_1$ space groups with a relative rotation angle of 13.2° around the crystallographic dyad. This rotation lengthens the x axis of form 2 from 264.49 Å to 293.38 Å and the z axis from 139.44 Å to 143.65 Å, and reduces the y axis from 71.19 Å to 64.01 Å. The volumes of the two unit cells differ by less than 2.5%. While superimposing only a monomer of form 1 on form 2, the other monomers of the dimer were related by a rotation of 1.2° and a translation of 0.14 Å. RMS difference due to superposition of the C_αs of a monomer between the two forms of MMOH is 0.27 Å. However, there is no noticeable change observed at the interface of the form 2 monomers compared with form 1 of the MMOH OB3b.

Differences between observed and predicted amino acid sequence

During the course of the map examination and model building, several places were found where the electron density map did not agree with the reported amino acid sequence inferred from the gene sequence (Cardy et al., 1991a, 1991b). These sites are shown in Figure 3 and fall into two classes. First, there are 15 randomly distributed sequence differences where the electron density map indicated a sequence more similar to that of MMOH Bath. For eight of these differences (Dα209E, Gα226A, Gα357A, Mβ255Y, Iβ256D, Dγ109E, Gγ109A, and Pγ160R), the published sequence (Cardy et al., 1991b) would have been sterically possible, but strong ($>5\sigma$) features in the $F_o - F_c$ maps and the definition of the $2F_o - F_c$ map left no doubt as to the discrepancy. Prominent in this group of differences is the change at α209 from aspartate to glutamate (see Fig. 2A,C) because this residue is a ligand of the diiron cluster. For seven of the differences, not only were the maps clear, but in three cases (Rα95G, insertion of Pα329, and Rγ88G) changes were required because the reported sequence was sterically impossible, and in four cases (Rα37W, Tα210A, Iα225S, and Vα331S), the reported residues were disfavored due to short steric contacts or the burying of unpaired charges.

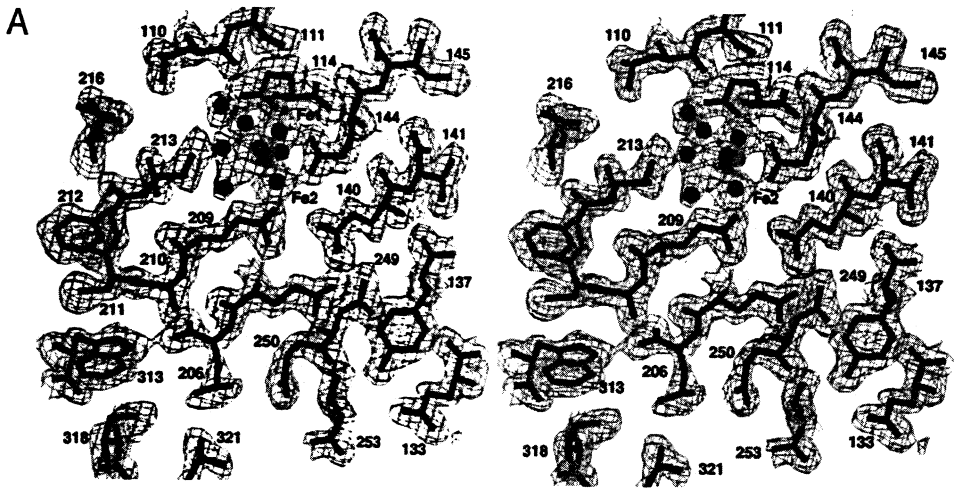
A
110
111
114
145
216
144
141
213
Fe2
140
212
209
210
249
137
211
250
313
206
318
321
253
133

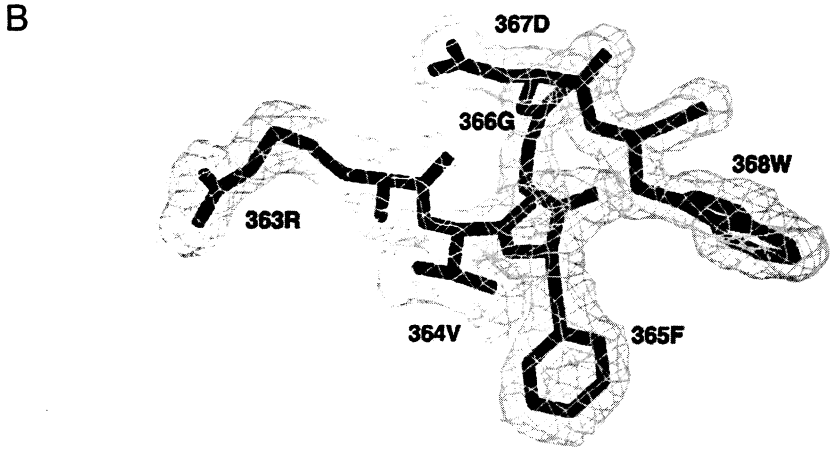
B
367D
366G
368W
363R
364V
365F

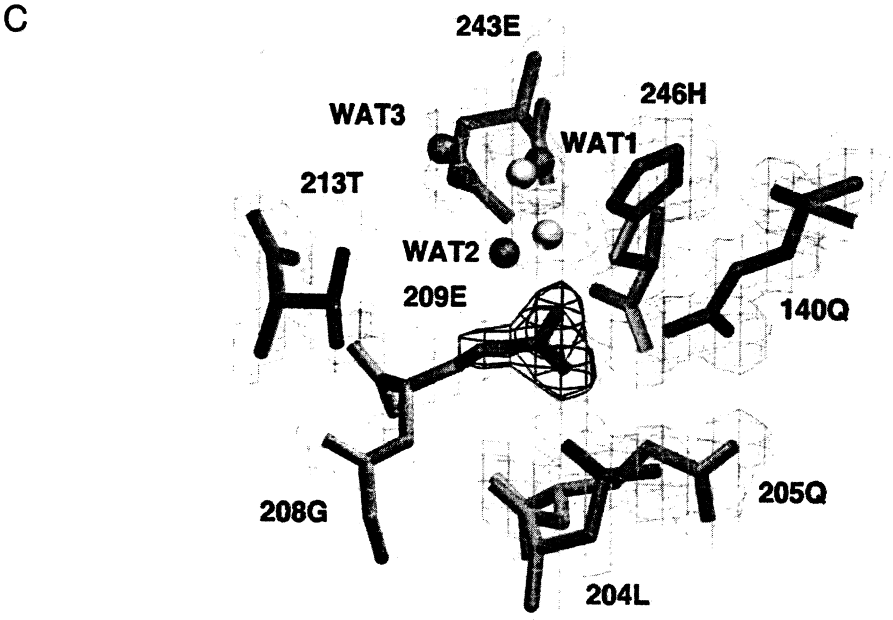
C
243E
246H
WAT3
WAT1
213T
WAT2
209E
140Q
208G
205Q
204L

Table 1. *Standard crystallographic data*

	Form 1	Form 2
Space group	$C222_1$	$C222_1$
Unit cell	a = 264.49 Å	a = 293.38 Å
	b = 71.19 Å	b = 64.01 Å
	c = 139.44 Å	c = 143.65 Å
Data collection		
Number of crystals	9	1
Number of reflections	391,667	177,040
Number of unique reflections	87,489	33,478
Completeness	96.8%	89.3%
R_{merge} of intensities[a]	0.075	0.094
Data used in final refinement		
Number of reflections	75,570	22,264
Cutoffs	5–2 Å, $F > 2\sigma$	5–2.7 Å, $F > 2\sigma$
Final R_{factor}[b]	0.137	0.152
Final R_{factor}[b] with $F > 0\sigma$	0.145	0.178
Model		
Number of protein atoms	8,599	8,599
Number of water molecules	731	2
Number of iron atom	2	2
Number of hydroxides	2	2
$\langle \lvert \Delta r \rvert \rangle$ from Luzzati plot	0.15 Å	0.20 Å
Stereochemistry		
RMS nonideal bond lengths	0.016 Å	0.013 Å
RMS nonideal bond angles	1.65°	1.61°
RMS dihedral angle	21.14°	21.39°
RMS improper angles	1.58°	1.54°
Themal parameters		
$\langle B \rangle$ for protein atoms	19.2 Å^2	18.5 Å^2
$\langle B \rangle$ for water molecules	37.1 Å^2	20.4 Å^2
$\langle B \rangle$ for iron and hydroxides	15.5 Å^2	27.6 Å^2

$$^{a}R_{merge} = \frac{\sum_{hkl}\sum_{i} |I_i(hkl) - \langle I(hkl)\rangle|}{\sum_{hkl}\sum_{i} I_i(hkl)}.$$

$$^{b}R_{factor} = \frac{\sum_{hkl} |F_{obs}(hkl) - F_{calc}(hkl)|}{\sum_{hkl} F_{obs}(hkl)}.$$

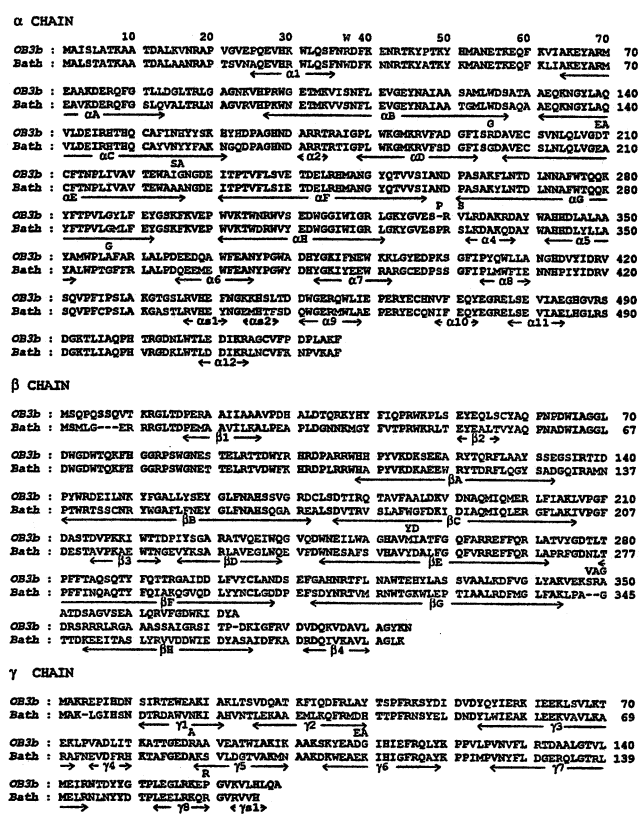

Fig. 3. Alignment of amino acid sequences of MMOH OB3b and MMOH Bath derived from the reported nucleotide sequences. Identical residues from both sequences are in black and the nonidentical residues are in red. Fe ligands are shown in cyan. Corrections to the amino acid sequence of MMOH OB3b determined by this work are shown in green above the aligned sequences. Secondary structural elements of MMOH OB3b are marked, with pairs of enclosing arrows, below the aligned sequences. All indicated elements are helices unless containing the letter "s" (β strands).

The second class of observed differences in the amino acid sequence is found near the carboxyl terminus of the β chain. This group of 26 consecutive differences is located at the top edge of the β chain as it is displayed in Figure 4. An examination of the published gene sequence corresponding to this region for MMOH OB3b (Cardy et al., 1991b) as shown in Figure 5 indicates that the observed amino acid sequence would be obtained if the base pair changes indicated in the figure occurred either through mutation of the strain or through sequencing errors. Figure 2B shows the excellent $2F_o - F_c$ electron density covering part of this polypeptide segment. All the sequence variations observed can be explained through the insertion, deletion, or change of one or two base pairs.

Active site of MMOH

The dinuclear iron cluster is located between the helices αB, αC, αE, and αF (see Figs. 2 and 4). As can be seen in Figure 6A, the ligands for both irons have octahedral geometry. The irons are separated by 2.99 Å, consistent with the Fe-Fe distance observed in recent EXAFS studies on MMOH (Shu et al., 1996a), the −160 °C MMOH Bath structure (Rosenzweig et al., 1995), and model complex studies (Thich et al., 1976; Borer et al., 1982; Zang et al., 1994). The irons are bridged by two hydroxides (or one hydroxide and one water), as well as a carboxylato-bridge from Glu α144. In the plane of the irons and the hydroxo ligands are four endogenous ligands: Glu α114, His α147, Glu α209, and His α246. Below this plane is the Glu α144 bridge. Above the plane, Wat 3 and Glu α243 complete the coordination sphere. As mentioned previously, Glu α209 is one of the residues where the observed sequence differed from that reported previously. Figure 2A and C shows the $2F_o - F_c$ electron density for the region around Glu α209.

The presence of a second bridging hydroxide (OH2) was indicated by a 5σ $F_o - F_c$ feature. However, because the $2F_o - F_c$

Fig. 2. (*Facing page*) Selected sections of $2F_o - F_c$ electron density map of the final model of MMOH OB3b contoured at 1σ. **A:** Portion of the active site and the adjacent hydrophobic cavity occupied by four water molecules. **B:** Residues β363–β368 of MMOH OB3b, a part of the 26 consecutive sequence corrections found in this region. **C:** A closeup view of the $2F_o - F_c$ (shown in light gray, contoured at 1σ) and $F_o - F_c$ electron density (shown in dark, contoured at 5σ) at α209 Glu. Side-chain atoms Cγ, Cδ, Oϵ1, Oϵ2 for residue α209 were omitted from the refinement and from the map calculation.

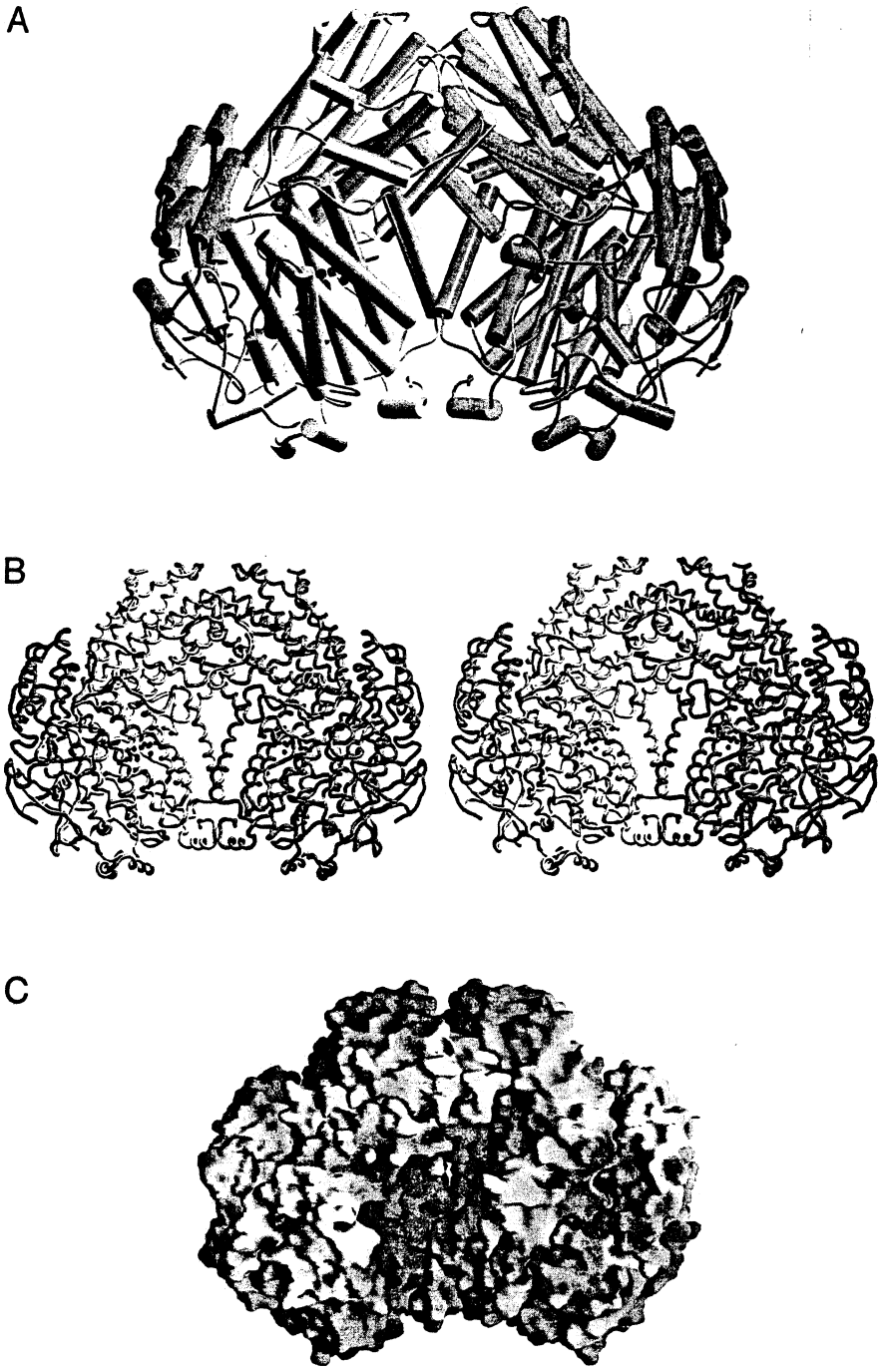

Fig. 4. Structure of MMOH OB3b. **A:** Secondary structure of dimer with cylinders representing the helices and arrows representing the β strands. The crystallographic twofold axis is vertical. α chains are colored yellow and pink, β chains are colored gray and cyan, and γ chains are green. Iron atoms are shown as green spheres, and the hydroxides and the water molecules at the active site, as well as those at the adjacent hydrophobic cavity, are shown as red spheres. **B:** Stereo drawing of C_α trace of dimer colored as in A. **C:** Solvent-exposed surface colored by electrostatic potential (red, negative; blue, positive) as calculated by GRASP (Nicholls et al., 1991).

density for OH2 was less clear than that for OH1, OH2 was not added to the model until late in the refinement. At that point, $F_o - F_c$ density calculated after omitting the OH2 showed a peak $>10\sigma$ and the feature could be accounted for in no other way. It was also confirmed by the difference map calculated using the final model coordinates after omitting the two hydroxides by setting their occupancies to zero and a cycle of refinement that showed 11σ peak at OH2 and 13σ peak at OH1. OH2 is held less tightly than OH1 as evidenced by the longer distances to the irons (2.15 Å and 2.17 Å versus 1.71 Å and 2.04 Å), weaker $2F_o - F_c$ density, and a slightly higher temperature factor (14.8 $Å^2$ versus 11.5 $Å^2$). It is not possible to distinguish between oxo, hydroxo, and aquo ligands from the electron density map. However, each of these potential bridging ligands have characteristic Fe-O bond lengths

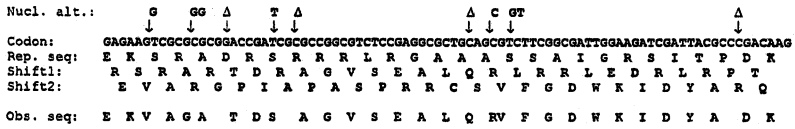

Fig. 5. Three reading frames of MMOH OB3b gene corresponding to residues β346–β375 are shown in lines "Rep. seq," "Shift1," and "Shift2." Sequence differences of the amino acids in the reported sequence (Cardy et al., 1991b) are shown in red in line "Rep. seq." Observed amino acids are shown in green. The corrected sequence from our study is also shown on the bottom line. Nucleotide sequence alterations required for the observed amino acid corrections are shown on top of the DNA strand. Δ stands for deletion of the nucleotide indicated. Nucleotide insertions are indicated by the other arrows.

that have been established from model studies. Bridging oxo ligands typically have Fe-O bond lengths of 1.7–1.9 Å (Kurtz, 1990), whereas the corresponding bond lengths for hydroxo and aquo bridging ligands are 1.9–2.1 Å (Armstrong & Lippard, 1984; Zang et al., 1994) and 2.15–2.3 Å (Hagen & Lachicotte, 1992), respectively. We assigned these two bridging atoms in the diiron cluster of MMOH OB3b as hydroxides based upon the observation that

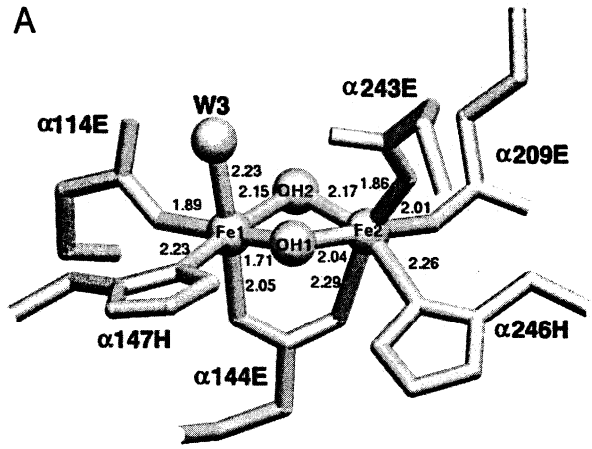

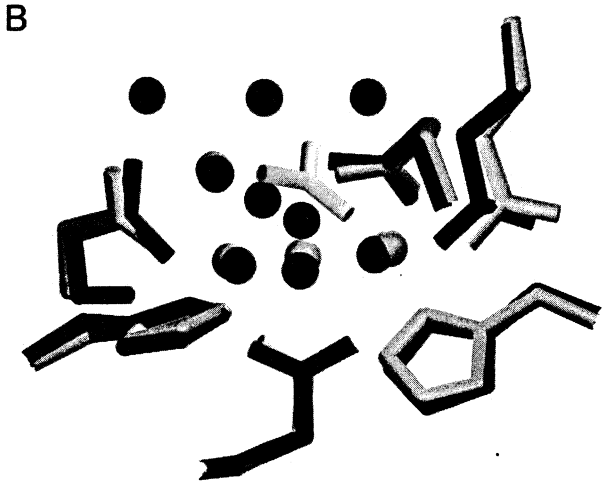

Fig. 6. Geometry of the diiron center. **A:** Diiron center in MMOH OB3b. **B:** Superposition of diiron center of one of the monomers of MMOH Bath at 4 °C (Rosenzweig et al., 1993) (shown in gray) onto that of MMOH OB3b at 18 °C (shown in black).

their average bond lengths to the ferric ions are at the minimum (1.91 Å) and maximum (2.15 Å) distances, respectively, expected for this type of bridge. The longer bond might also be assigned to an aquo bridge, but the aquo bridge observed in the MMOH Bath diiron cluster in this position has a considerably longer average bond length (2.4 Å), suggesting that the bond in the current structure derives from a bridging hydroxo ligand. Moreover, the short Fe-Fe distance is more consistent with a hydroxo than an aquo bridge (Hagen & Lachicotte, 1992). The assignment of the shorter bonds as an oxo bridging ligand is disfavored on the basis that no optical spectrum is observed from the cluster in the spectral region expected for well-characterized oxo-bridged diiron clusters (Fox et al., 1989; Kurtz, 1990). Moreover, the exchange coupling observed for the cluster is much smaller than that of any known oxo-bridged diiron cluster (Fox et al., 1993).

Above and behind the diiron cluster, as oriented in Figure 6, is a hydrophobic cavity (volume 70 Å^3) lined by Leu α10, Gly α13, Ala α117, Ala α120, Gln α140, Cys α151, Ala α152, Ile α171, Met α184, Phe α188, Phe α192, Leu α204, Thr α213, Leu α216, Ile α217, Phe α236, Val α239, Gln α278, and Phe α282. In this cavity, there is a region of $2F_o - F_c$ density that is not due to protein and has proven difficult to assign to a specific exogenous molecule (see Fig. 2A). During the refinement, we attempted to place several molecules in this density, including phosphate, because it was the only component in the crystallization solution of the appropriate size, but none were found to fit satisfactorily. Other obvious species that were placed initially in the density were methane and methanol; however, a single molecule was too small for the density and multiple molecules did not seem to fit the density very well. Because no species fit the density well, four solvent molecules (Wat 4, Wat 5, Wat 6, and Wat 7) were finally placed in the density. The average *B*-factor for these four water molecules is 40.0 Å^2, which is comparable to 37.1 Å^2, the average *B*-factor for all the water molecules in the structure.

Comparison with MMOH Bath

The high level of sequence identity of MMOH OB3b with MMOH Bath (see Fig. 3) suggests that similar structures will be observed, and this is the case. It should be mentioned here that the MMOH OB3b crystallizes as a monomer per asymmetric unit. Thus, the crystallographic twofold symmetry requires exact symmetry in the holoenzyme of MMOH OB3b. MMOH Bath crystallizes as a dimer in an asymmetric unit with noncrystallographic twofold symmetry restraints relating the monomers. It is not stated in either of the reports (Rosenzweig et al., 1993, 1995) or the PDB entry 1MMO whether noncrystallographic symmetry restraints were used during refinement of MMOH Bath. Superposition of the C_αs of the MMOH Bath monomers produces an RMS difference of 0.28 Å.

Superposition of the two protomers of MMOH Bath found in its asymmetric unit with the crystallographic dimer found in the MMOH OB3b unit cell results in an RMS difference over all C_αs of 0.76 Å. Superposition of the individual monomers reduces this difference to 0.56 Å. The largest differences (those greater than 1.5 Å) between MMOH OB3b and MMOH Bath for the C_α trace are found at the terminal residues, and at residues α340, α349, α430–α435, β32–β40, β47, β250–β280, β325–β330, and β338–β354. The most significant changes observed are in the region β345–β354, corresponding to residues β341–β350 of MMOH Bath. This region is on the outer surface of the molecule and is not involved in any intermolecular contacts in either of the MMOHs. In MMOH Bath, the closest neighbor to this region consists of residues β377–β385 of the symmetry-related molecule, whereas in MMOH OB3b, the corresponding residues from the symmetry-related molecule are γ88–γ100. The shortest distance between the molecule and the symmetry-related molecule at this interface for MMOH Bath is 3.93 Å, whereas that for MMOH OB3b is 3.68 Å. In both MMOHs, the C-terminal residue of the β chain is in this interface. In OB3b, there is a piece of continuous electron density that extends beyond the structurally derived last residue of the β chain (β393) in the final model. However, the last two residues of the β chain (Lys β394 and Asn β395) could not be modeled due to very short contacts between the side chains of these two residues and the γ chain of the neighboring symmetry-related molecule. Hence, this region of density at the interface is modeled as four water molecules (Wat 699, Wat 729, Wat 730, and Wat 731).

The superposition of the structures of the diiron clusters of MMOH OB3b and that of one of the noncrystallographically related protomers of MMOH Bath (4 °C structure) are shown in Figure 6B. Overall, the active sites of both hydroxylases are quite similar. With the correction of Glu α209, the protein ligand backbones agree with an RMS difference of 0.16 Å (averaged for both monomers of MMOH Bath). This difference is comparable to that seen between MMOH Bath protomers (0.10 Å). Superposition of the diiron cluster ligands and the residues that line the hydrophobic cavity gives an RMS difference for the backbone atoms between MMOH OB3b and MMOH Bath of 0.19 Å (averaged for both the monomers of MMOH Bath), which is again comparable to that between the monomers of MMOH Bath (0.13 Å). With this level of structural similarity, the significantly higher specific activity for MMOH OB3b (Fox et al., 1989) cannot be explained easily by differences in active site structure. More specifically, the difference does not derive from the residue at position 209, as suggested previously by Rosenzweig et al. (1993), because this residue is shown here to be the same in both enzymes.

The diiron clusters of the two MMOHs do exhibit some significant differences in distance between the iron atoms and the exogenous bridging ligands. Table 2 lists the bond lengths and angles of the active site structure of MMOH OB3b for both form 1 and 2, and those of the two protomers of MMOH Bath at 4 °C and −160 °C (Rosenzweig et al., 1993, 1995). The major differences between the 4 °C MMOH Bath diiron cluster structure and that of MMOH OB3b is the longer Fe-Fe distance and the presence of an acetate (rather than a hydroxide) as the second exogenous bridge in the MMOH Bath cluster. In contrast, in the MMOH Bath structure determined at −160 °C (Rosenzweig et al., 1995), the Fe-Fe distance and exogenous bridging ligands are in excellent agreement with those seen for MMOH OB3b. Rosenzweig et al. (1995) argue that the geometry seen in the −160 °C structure might be the result of including glycerol in the mother liquor as a cryoprotectant; but the results reported here for MMOH OB3b suggest that this is not the case. The similarity of the −160 °C MMOH Bath and the 18 °C MMOH OB3b structures suggests that the Fe_2-O_2 diamond core that they have in common may be a general feature of MMOHs.

Recent evidence suggests similarities in structure and reactivity between synthetic model compounds containing high valent Fe_2O_2 diamond core dinuclear iron complexes (Dong et al., 1995a, 1995b; Que & Dong, 1996) and the reactive high valent intermediate **X** of the R2 subunit of ribonucleotide reductase and compound Q of the MMOH catalytic cycle (Lee et al., 1993a, 1993b; Sturgeon et al., 1996). This resemblance suggests that the ability to form such a structure is important for the oxygen activation and insertion reactions that are catalyzed. On the other hand, EXAFS studies of the diferric MMOH OB3b (Shu et al., 1996a) indicate that, in frozen solution, about 40% of clusters have a 3.4-Å Fe-Fe distance, similar to the 4 °C MMOH Bath structure, whereas the remainder have a 3.0-Å Fe-Fe distance, similar to the −160 °C MMOH Bath and 18 °C MMOH OB3b structures. Consequently, all of the structures determined thus far for MMOH may be valid for the enzyme in solution under certain circumstances and may be indicative of the inherent flexibility of the cluster. Such flexibility may be nec-

Table 2. *Bond distances and angles of the diamond core found in MMO hydroxylases*

	OB3b		Bath	
	Form 1	Form 2		
Temperature	18 °C	18 °C	4 °C	−160 °C
Fe-Fe distance	2.99 Å	3.07 Å	3.46 Å, 3.36 Å	3.04 Å, 3.14 Å
First bridge	OH	OH	OH	OH
Fe1-OH	1.71 Å	1.79 Å	1.71 Å, 1.69 Å	1.78 Å, 1.62 Å
Fe2-OH	2.04 Å	2.18 Å	1.98 Å, 2.06 Å	1.94 Å, 2.02 Å
Angle Fe1-OH-Fe2	105.4°	100.8°	138.6°, 127.7°	109.0°, 120.0°
Second bridge	OH	OH	CH_3COOH	H_2O
Fe1-OH	2.15 Å	1.93 Å	2.56 Å, 1.95 Å	2.43 Å, 2.24 Å
Fe2-OH	2.17 Å	2.45 Å	2.30 Å, 2.05 Å	2.58 Å, 2.51 Å
Angle Fe1-OH-Fe2	87.6°	88.1°	N/A	Not reported

[a]Bath data for the 4 °C structure are derived from the PDB entry 1MMO, and those for −160 °C are from Rosenzweig et al. (1995).

essary to accommodate various intermediates of the catalytic cycle that appear to have quite different diiron core structures. These intermediates range from the proposed peroxo-bridged compound P, which may require an Fe-Fe distance of up to 4 Å (Kim & Lippard, 1996), to the proposed diamond core bridged compound Q, in which the Fe-Fe distance is 2.47 Å (Shu et al., 1996b).

Electron density maps for both MMOH OB3b and MMOH Bath at −160 °C indicate the presence of some exogenous molecule(s) in the active site of MMOH. In the case of MMOH Bath, this density was interpreted as that of acetate, because acetate was present in the crystallization solutions (Rosenzweig et al., 1992). It is doubtful that acetate is the component present in the active site of MMOH OB3b because acetate is not in any of the solutions used for protein purification or crystallization. As mentioned previously, the unassigned density has been filled tentatively by four water molecules; however, this density cannot be unambiguously assigned at present for either enzyme.

Comparison with cytochrome P-450$_{CAM}$ and other diiron proteins

MMOH has been compared widely to cytochrome P-450, because it also activates molecular oxygen for incorporation into many substrates containing unactivated C-H bonds. In both enzymes, iron centers are reduced to allow the binding of molecular oxygen. The oxygen is then cleaved to produce water and a high valent reactive iron-oxo species that is capable of breaking a stable C-H bond (Ortiz de Montellano, 1986; McMurry & Groves, 1986; Lipscomb, 1994). In the case of cytochrome P-450, it has been proposed that breaking the O-O bond of oxygen requires protons to be shuttled into the active site to form water from one of the oxygen atoms as the high valent reactive species is formed. If the mechanism of MMO is fundamentally similar to that of cytochrome P-450, as we have proposed (Fig. 1, Fox et al., 1989, 1991), then a similar residue might be expected to be present in the active site of MMO to facilitate proton transfer. Because the only residues with side chains capable of forming hydrogen bonds in the active site of MMOH are Thr α213 and Cys α151 (see Figs. 2A and 7A), one of these residues could be involved in the proton transfer. In cytochrome P-450$_{CAM}$ (Poulos et al., 1985), Thr 252 Oγ is 5.7 Å from the heme iron. This distance compares with 6.3 Å and 6.8 Å for Thrα 213 Oγ from Fe1 and Fe2 of MMOH, respectively. Figure 7B shows the active site of cytochrome P-450$_{CAM}$ oriented to emphasize this similar geometry. Mutation of Thr 252 to Ala in cytochrome P-450 uncouples the ability of this enzyme to hydroxylate substrate, with little or no product being formed (Imai et al., 1989; Martinis et al., 1989). Comparison of the amino acid sequences of MMOH with the diiron containing enzymes toluene 4-monooxygenase, phenol hydroxylase, and the stearoyl-ACP desaturases (Fox et al., 1994) reveals that the residue corresponding to α213 is always a threonine.

It has been suggested that a cysteinyl radical at Cys α151 might play a role in the hydroxylation chemistry at the active site of MMOH (Nordlund et al., 1992; Rosenzweig et al., 1993; Feig & Lippard, 1994). A basis for this suggestion can be seen by comparing the diiron centers of MMOH and of the R2 subunit of ribonucleotide reductase. As seen in Figure 7C, the residue corresponding to Cys α151 of MMOH is Tyr 122 of ribonucleotide reductase R2, which is the site of the stable tyrosyl radical generated by reaction of the dinuclear iron cluster of the protein. However, the amino acid sequence of toluene 4-monooxygenase has a glutamine in the homologous position, whereas the stearoyl-ACP desaturases have leucine (Fox et al., 1994). This suggests that Cys α151 may not be critical to catalytic function.

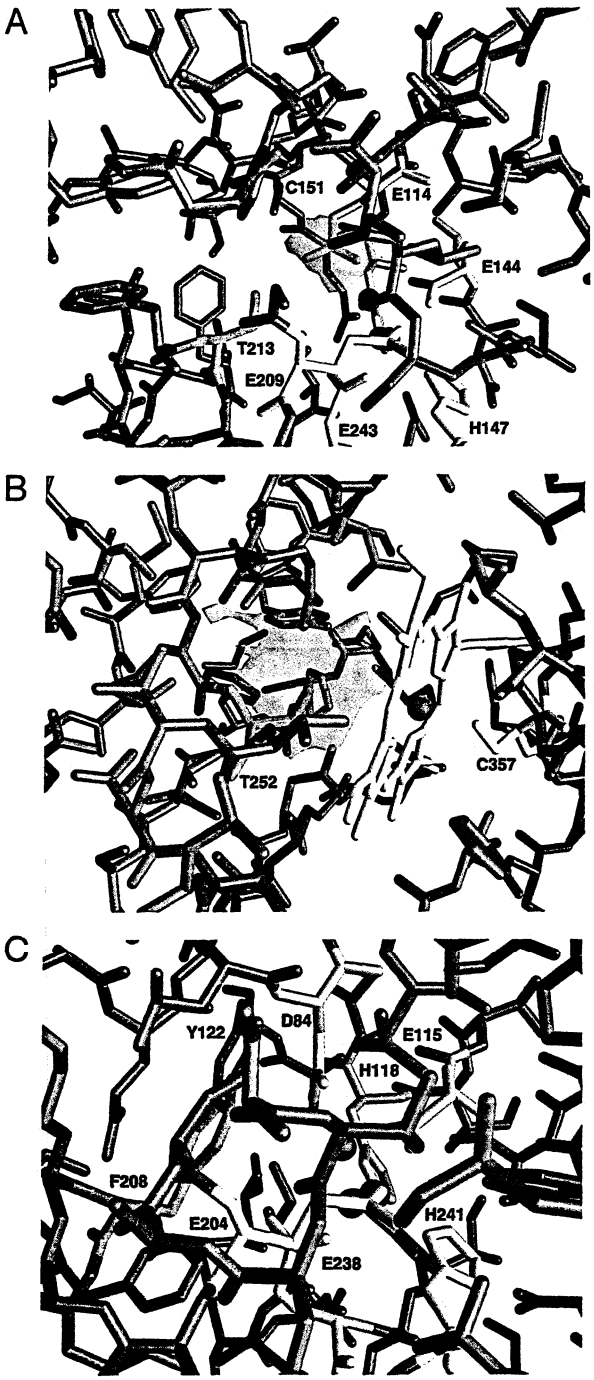

Fig. 7. Active sites of (A) MMOH OB3b, (B) cytochrome P-450$_{CAM}$, and (C) ribonucleotide reductase R2 protein. Iron is shown in red and the hydroxide is shown in green as spheres. Residues corresponding to Cys α151 of MMOH OB3b are orange, those corresponding to Thr α213 are green, and those ligating the iron are yellow. The solvent-accessible surface near the iron(s) is shown with a transparent cyan surface.

Effects of component B

As stated earlier, component B was included in the crystallization solution that generated crystal form 2. Component B. by forming a tight complex with MMOH, has many significant effects on the activity of MMO that were summarized in the introduction (Fox et al., 1991; Wallar & Lipscomb, 1996). Both steady state and transient kinetic studies show that optimal rate enhancements are achieved when the bound complex stoichiometry is 2 MMOB:1 MMOH, that is, 1 MMOB per protomer or active site. Despite the fact that MMOB was present in a 2:1 stoichiometry during crystallization and a new crystal form was obtained, the electron density map showed no density for component B in the crystal structure. Moreover, SDS-PAGE of washed form 2 crystals indicated that component B was not present.

Growth of the crystal form 2 required the presence of component B. Duplicate crystallization trials under the same conditions except that component B was absent did not produce crystals. Previous studies have indicated (1) that interaction of MMOB and MMOH alters the MMOH structure and (2) that these alterations reverse slowly after dissociation of the complex (Fox et al., 1991; Froland et al., 1992; Liu et al., 1995a; Y. Liu, J. Nesheim, K.E. Paulsen, M.T. Stankovich, & J.D. Lipscomb, manuscript submitted). This hysteretic effect may cause a general change in the structure of the population of MMOH in the presence of MMOB, which is required to nucleate crystal form 2. In form 2 crystal structure, the dimer is rotated by 13.2° around the crystallographic *a* axis, with a 1.2° rotation of one monomer relative to the other from the crystallographic dyad with respect to form 1. Superposition of the monomers observed in both crystal forms produces an RMS difference of 0.60 Å over all atoms. Because this difference is comparable to that observed in independent refinements of the same protein (Ohlendorf, 1994), the structural changes imparted by component B binding are either too subtle to be seen at 2.4 Å resolution or have decayed back to native state.

An examination of the solvent-exposed surface of MMOH (Fig. 4C) reveals a negatively charged depression approximately 35 Å in diameter to the left of the twofold axis and directly above helices A, E, and F. Helices E and F participate in the active site by supplying three iron ligands (α209, α243, and α246) and by forming half of the active site pocket occupied by Wat 699, Wat 729, Wat 730, and Wat 731. Helix E is bent into three fragments (α197–α204, α208–α211, and α213–α226). By binding to this region, component B could alter the iron ligand geometry, as well as the volume of the active site, and thus modulate activity.

Conclusions

The observation of a diamond core structure for the essential diiron cluster of the active site of MMOH OB3b similar to that reported for the −160 °C structure of MMOH Bath shows that this is the dominant structure that has been maintained across the family of sMMO enzymes from highly divergent methanotrophs. Moreover, the presence of the diamond core structure in the highly active *M. trichosporium* MMOH that has been crystallized and studied at near room temperature strongly supports this conclusion. The diamond core structure is probably lost during some stages of the catalytic cycle, but it appears to be the most likely structure for the critical transient intermediate, compound Q, that appears to insert oxygen into the unactivated C-H bond of methane. The significance of the compact diamond core structure to oxygen activation and insertion chemistry is currently under intense investigation (Que & Dong, 1996). This novel structure presents many mechanistic possibilities beyond those considered in the past for heme oxygenases (Feig & Lippard, 1994; Wallar & Lipscomb, 1996). The structural insight provided by the current study supports the occurrence of such a species in MMOH catalysis and supplies critical metric information for ongoing biomimetic studies.

Materials and methods

Crystal form 1

The growth of *M. trichosporium* OB3b and the purification of MMOH were as reported previously (Fox et al., 1989, 1990a). The specific activity at 23 °C and iron content of MMOH OB3b are 800–1000 nmol/min/mg and 1.8–2.0 diiron clusters/mol, respectively. Diffraction-quality crystals were obtained as reported by a hanging drop method with repeated macroscopic seeding at 18 °C (Froland et al., 1994). Typical crystal size is 0.7 mm × 0.7 mm × 0.3 mm. The crystals are in space group $C222_1$, with one monomer per asymmetric unit. X-ray data were collected using a MAR imaging plate mounted on beamline X12C at the Brookhaven National Laboratory. Images were processed using DENZO (Otwinowski, 1993). Although diffraction to about 2.5 Å resolution was resistant to radiation damage, the higher-resolution data (to <1.8 Å resolution) had a lifetime of about 1 h on X12C. Consequently, a high-resolution native data set was formed using data collected from nine crystals of MMOH OB3b.

Coordinates of one protomer of MMOH Bath (Rosenzweig et al., 1993) (chains B, D, and G) were extracted from the PDB data file 1MMO. Using these coordinates, a cross rotation function was calculated with XPLOR (Brünger, 1992). Two searches, each with vector lengths of 45 Å and 35 Å, were conducted using data between 8 and 3.5 Å and 8 and 4 Å. Both searches yielded the same prominent peak that, following Patterson correlation refinement, gave a peak that was 9.7 times higher than the next highest peak. Coordinates corresponding to this peak were used in the translation-search by XPLOR. This resulted in a single solution and provided an initial model for MMOH OB3b. After setting aside 2% (1,721 reflections) of the observed data for the calculation of R_{free}, molecular dynamics refinement by simulated annealing using XPLOR reduced the *R*-factor and R_{free} for data between 8–2.8 Å, with $F > 2\sigma$, to 24.8% and 34.5%, respectively. Because the values of R_{free} and *R* indicated a correct solution, all the data were used in the subsequent refinements and map calculations. Group temperature factor refinement using the data between 8 and 3.5 Å resolution and $F > 3\sigma$ produced an *R*-factor of 21.7%. Using TOM (Jones, 1978), this model was examined and the sequence of the model was altered to that expected for MMOH OB3b (Cardy et al., 1991b). Several cycles of Powell minimization were run at varying resolutions trying to reconcile the model with the expected amino acid sequence. When this failed, residues that disagreed with the published sequence were replaced with either alanines or glycines and main-chain breaks were made at the points of residue insertions. Additional cycles of refinement accompanied by phase extension to 2 Å resolution with $F > 2\sigma$ converged to an *R*-factor of 22.2%. By this time, several of the randomly distributed sequence changes reported in Figure 3 had been made and clear density for solvent molecules was apparent. After adding 230 water molecules with a polyalanine model for β345–β372, the *R*-factor dropped to 19.0% for data between 5 and 2 Å, with $F > 2\sigma$. At this point, an examination of the reading frames for the β chain of

MMOH produced an amino acid sequence that agreed with that seen in the electron density maps. In addition, the density now unambiguously indicated the presence of the second bridging hydroxide. Further refinement after these corrections and adding another 200 water molecules reduced the *R*-factor to 16.2% for data between 5 and 2 Å, with $F > 2\sigma$. During the next cycles of map examination, addition of solvent molecules, and refinement, various models (a phosphate, two methanols with half occupancies each occupying alternating confirmations, two methanes, an ethanol, an ethane, a serine, a cysteine) were tested in the density feature found in the active site. Because no single model explained this density adequately, a group of four solvents was placed in the model, which, on refinement, produced an *R*-factor of 14.4% for data between 5 and 2 Å, with $F > 2\sigma$. Additionally, two water molecules were found on special positions. On inclusion of these water molecules, refinement produced an *R*-factor of 13.7% for the final model for data between 5 and 2.0 Å, with $F > 2\sigma$ (14.5% with no cut off).

Crystal form 2

The growth of *M. trichosporium* OB3b and purification of MMOH and MMOB were as reported previously (Fox et al., 1989, 1990a). The specific activity at 23 °C of MMOB was 7,000 nmol/min/mg. Single form 2 crystals were obtained by vapor diffusion starting with a 10 mg/mL mixture of MMOH OB3b and recombinant MMOB with a molar ratio of 2 MMOB:1 MMOH OB3b. The reservoir solution consisted of 18% (w/v) PEG_{3350}, 167 mM Na_2HPO_4, and 10 mM citric acid at pH 7.5. After combining 7 μL of the MMOH/component B mixture with 7 μL of the mother liquor (4% PEG_{3350} and 100 mM phosphate/citrate buffer, pH 7.7), large single crystals were obtained after 16 days. The crystals are in space group $C222_1$, with one monomer per asymmetric unit. A native data set was collected to 2.71 Å resolution using a Siemens/Xentronics X100 area detector mounted on a Rigaku rotating anode source.

A nearly completely refined model of MMOH OB3b was used as a search model for molecular replacement in the program XPLOR (Brünger, 1992). The rotational search produced a peak that, after Patterson correlation refinement, was 8.1 times higher than the next highest peak. Coordinates corresponding to this peak were used in the translation search by XPLOR. This resulted in a single solution and provided an initial model for the form 2 of MMOH OB3b. After setting aside 5% (1,658 reflections) of the observed data for the calculation of R_{free}, molecular dynamics refinement by simulated annealing using XPLOR produced a model with an *R*-factor of 19.2% and R_{free} of 29.3% for data between 8 and 2.8 Å, with $F > 2\sigma$. Because the values of R_{free} and *R* indicated that the solution was correct, all the data were used for further refinement and map calculations. Group temperature-factor refinement using data between 8 and 2.7 Å and $F > 2\sigma$ brought down the *R*-factor to 17.3%. Powell minimization using XPLOR produced a model with an *R*-factor of 16.7% for data between 8 and 2.7 Å, with $F > 2\sigma$. Examination of the electron density map, addition of the two Fe^{3+}, the two bridging hydroxides, and the exogenous ligand (one water molecule) to the iron, and Powell minimization using XPLOR produced a model with a crystallographic *R*-factor of 16.3% using 22,264 unique reflections between 5 and 2.7 Å resolution, with $F > 2\sigma$. *B*-factors were found as low as 2 $Å^2$ for many of the side-chain atoms. Hence, *B*-factors for the whole model were reset to the Wilson *B*-factor before the next cycle of refinement. At this stage, the two bridging hydroxides had poor $2F_o - F_c$ density, which we attribute to the lower-resolution data of the diffraction. Even though the $2F_o - F_c$ as well as positive $F_o - F_c$ density was obvious for about 240 water molecules, none were placed in the model except one water molecule at the hydrophobic cavity because of the limited resolution. The complete model was checked and a final set of positional and temperature-factor refinement produced an *R*-factor of 15.2% for the final model for data between 5 and 2.7 Å, with $F > 2\sigma$ (17.8% with no cut off).

During refinement of both crystal forms of MMOH OB3b, NOE square well constraints were placed on the irons and their ligands. For crystal form 1, the Fe-ligand NOEs were set to 2.0 ± 0.4 Å and the Fe-Fe NOE was set to 3.0 ± 0.4 Å. For crystal form 2, the NOEs were set to the values observed in crystal form 1 (±0.4 Å). Coordinates of both forms of the crystal structure of MMOH OB3b have been submitted to Protein Data Bank with accession numbers 1MHY and 1MHZ.

Figures 2, 4A, 4B, and 6 were made using SETOR (Evans, 1993). Figures 4C and 7 were made using GRASP (Nicholls et al., 1991).

Acknowledgments

This work was supported in part by NIH grants GM40466 (J.D.L.), GM46436 (D.H.O.), NSF grant MCB 9220024 (D.H.O.), and an NIH predoctoral training grant GM08277 (B.J.W., W.A.F.). We also acknowledge the Minnesota Supercomputer Institute for use of the CRAY-YMP, Brookhaven National Laboratory for use of beamline X12C of the National Synchrotron Light Source for X-ray data collection, and David H. Dyer for technical assistance.

References

Andersson KK, Froland WA, Lee SK, Lipscomb JD. 1991. Dioxygen independent oxygenation of hydrocarbons by methane monooxygenase hydroxylase component. *New J Chem 15*:411–415.

Anthony C. 1982. *The biochemistry of the methylotrophs*. London, UK: Academic Press.

Armstrong WH, Lippard SJ. 1984. Reversible protonation of the oxo bridge in a hemerythrin model compound. Synthesis, structure, and properties of (μ-hydroxo) bis(μ-acetato)-bis[hydrotris(1-pyrazoly)borato]diiron(III), $[HB(pz)_3Fe(OH)(O_2)CCH_3)_2Fe(HB(pz)_3)]^+$. *J Am Chem Soc 106*:4632–4633.

Borer L, Thalken L, Ceccarrelli C, Glick M, Zhang JH, Reiff WM. 1983. Synthesis and characterization of a hydroxyl-bridged iron(III) dimer of N,N′-ethylenebis(salicylamine). *Inorg Chem 22*:1719–1724.

Brünger AT. 1992. *XPLOR, version 3.1. A system for X-ray crystallography and NMR*. New Haven, Connecticut: Yale University Press.

Cardy DLN, Laidler V, Salmond GPC, Murrell JC. 1991a. The methane monooxygenase gene cluster of *Methylosinus trichosporium*: Cloning and sequencing of mmoC gene. *Arch Microbiol 156*:477–483.

Cardy DLN, Laidler V, Salmond GPC, Murrell JC. 1991b. Molecular analysis of the methane monooxygenase (MMO) gene cluster of *Methylosinus trichosporium* OB3b. *Mol Microbiol 5*:335–342.

Colby J, Stirling DI, Dalton H. 1977. The soluble methane monooxygenase of *Methylococcus capsulatus* Bath: Its ability to oxygenate n-alkanes, n-alkenes, ethers and alicyclic, aromatic and heterocyclic compounds. *Biochem J 165*:395–402.

Dalton H. 1980. Oxidation of hydrocarbons by methane monooxygenases from a variety of microbes. *Adv Appl Microbiol 26*:71–87.

Dalton H. 1991. Structure and mechanism of action of the enzymes involved in methane oxidation. In: Kelly JW, Baldwin T, eds. *Applications of enzyme biotechnology*. New York: Plenum. pp 55–68.

DeRose VJ, Liu KE, Kurtz DM Jr, Hoffman BM, Lippard SJ. 1993. Proton ENDOR identification of bridging hydroxide ligands in mixed-valent diiron centers of proteins: Methane monooxygenase and semimet azidohemerythrin. *J Am Chem Soc 115*:6440–6441.

DeWitt JG, Bentsen JG, Rosenzweig AC, Hedman B, Green J, Pilkington S, Papaefthymiou GC, Dalton H, Hodgson KO, Lippard SJ. 1991. X-ray ab-

sorption, Mossbauer, and EPR studies of the dinuclear iron center in the hydroxylase component of methane monooxygenase. *J Am Chem Soc 113*:9219–9235.

Dong Y, Fujii H, Hendrich MP, Leising RA, Pan G, Randall CR, Wilkinson EC, Zang Y, Que L Jr, Fox BG, Kauffmann K, Münck E. 1995a. A high-valent nonheme iron intermediate. Structure and properties of $[Fe_2(\mu\text{-}O)_2(5\text{-}Me\text{-}TPA)_2](ClO_4)_3$. *J Am Chem Soc 117*:2778–2792.

Dong Y, Que L Jr, Kauffmann K, Münck E. 1995b. An exchange-coupled complex with localized high-spin Fe^{IV} and Fe^{III} sites relevance to cluster X of *Escherichia coli* ribonucleotide reductase. *J Am Chem Soc 117*:11377–11378.

Evans SV. 1993. SETOR: Hardware lighted three-dimensional solid model representations of macromolecules. *J Mol Graphics 11*:134–138.

Feig AL, Lippard SJ. 1994. Reactions of non-heme iron(II) centers with dioxygen in biology and chemistry. *Chem Rev 94*:759–805.

Fox BG, Borneman JG, Wackett LP, Lipscomb JD. 1990b. Haloalkene oxidation by the soluble methane monooxygenase from *Methylosinus trichosporium* OB3b: Mechanistic and environmental implications. *Biochemistry 29*:6419–6427.

Fox BG, Froland WA, Dege J, Lipscomb JD. 1989. Methane monooxygenase from *Methylosinus trichosporium* OB3b: Purification and properties of a three component system with high specific activity from a type II methanotroph. *J Biol Chem 264*:10023–10233.

Fox BG, Froland WA, Jollie DR, Lipscomb JD. 1990a. Methane monooxygenase from *Methylosinus trichosporium* OB3b. *Methods Enzymol 188*:191–202.

Fox BG, Hendrich MP, Surerus KK, Andersson KK, Froland WA, Lipscomb JD, Münck E. 1993. Mossbauer, EPR, and ENDOR studies of the hydroxylase and reductase components of methane monooxygenase from *Methylosinus trichosporium* OB3b. *J Am Chem Soc 115*:3688–3701.

Fox BG, Liu Y, Dege, JE Lipscomb JD. 1991. Complex formation between the protein components of methane monooxygenase from *Methylosinus trichosporium* OB3b. Identification of sites of component interaction. *J Biol Chem 266*:540–550.

Fox BG, Shanklin J, Ai J, Loehr TM, Sanders-Loehr J. 1994. Resonance Raman evidence for an Fe-O-Fe center in stearoyl-ACP desaturase. Primary sequence identity with other diiron-oxo proteins. *Biochemistry 33*:12776–12786.

Fox BG, Surerus KK, Münck E, Lipscomb JD. 1988. Evidence for a μ-oxo-bridged binuclear iron cluster in the hydroxylase component of methane monooxygenase. *J Biol Chem 263*:10553–10556.

Froland WA, Andersson KK, Lee SK, Liu Y, Lipscomb JD. 1992. Methane monooxygenase component B and reductase alter the regioselectivity of the hydroxylase component-catalyzed reactions. A novel role for protein–protein interactions in an oxygenase mechanism. *J Biol Chem 267*:17588–17597.

Froland WA, Dyer DH, Radhakrishnan R, Earhart CA, Lipscomb JD, Ohlendorf DH. 1994. Preliminary crystallographic analysis of methane monooxygenase hydroxylase from *Methylosinus trichosporium* OB3b. *J Mol Biol 236*:379–381.

Green J, Dalton H. 1989. Substrate specificity of soluble methane monooxygenase: Mechanistic implications. *J Biol Chem 264*:17698–17703.

Hagen KS, Lachicotte R. 1992. Diiron(II) μ-aqua bis(μ-carboxylato) models of reduced dinuclear non-heme iron sites in proteins. *J Am Chem Soc 114*:8741–8742.

Higgins IJ, Best DJ, Hammond RC. 1980. New findings in methane-utilizing bacteria highlight their importance in the biosphere and their commercial potential. *Nature 286*:561–564.

Imai M, Shimada H, Watanabe Y, Matsushima-Hibiya Y, Makino R, Koga H, Horiuchi T, Ishimura Y. 1989. Uncoupling of the cytochrome $P\text{-}450_{CAM}$ monooxygenase reaction by a single mutation, threonine-252 to alanine or valine: Possible role of the hydroxy amino acid in oxygen activation. *Proc Natl Acad Sci USA 86*:7823–7827.

Jones TA. 1978. A graphics model building and refinement system for macromolecules. *J Appl Crystallogr 11*:268–272.

Kim K, Lippard SJ. 1996. Structure and Mossbauer spectrum of a (μ-1,2-peroxo) bis(μ-carboxylato) diiron(III) model for the peroxo intermediate in the methane monooxygenase hydroxylase reaction cycle. *J Am Chem Soc 118*:4914–4915.

Kurtz DM Jr. 1990. Oxo and hydroxo-bridged diiron complexes: A chemical perspective on a biological unit. *Chem Rev 90*:585–606.

Laskowski RA, MacArthur MW, Moss DS, Thornton JM. 1993. PROCHECK: A program to check stereochemical quality of protein structures. *J Appl Crystallogr 26*:283–291.

Lee SK, Fox BG, Froland WA, Lipscomb JD, Münck E. 1993a. A transient intermediate of the methane monooxygenase catalytic cycle containing a $Fe^{IV}Fe^{IV}$ cluster. *J Am Chem Soc 115*:6450–6451.

Lee SK, Nesheim JC, Lipscomb JD. 1993b. Transient intermediates of the methane monooxygenase catalytic cycle. *J Biol Chem 268*:21569–21577.

Lipscomb JD. 1994. Biochemistry of the soluble methane monooxygenase. *Annu Rev Microbiol 48*:371–399.

Liu KE, Valentine AM, Qiu D, Edmondson DE, Appelman EH, Spiro TG, Lippard SJ. 1995a. Characterization of a diiron(III) peroxo intermediate in the reaction cycle of methane monooxygenase hydroxylase from *Methylococcus capsulatus* (Bath). *J Am Chem Soc 117*:4997–4998.

Liu KE, Valentine AM, Wang DL, Huynh BH, Edmondson DE, Salifoglou A, Lippard SJ. 1995b. Kinetic and spectroscopic characterization of intermediates and component interactions in reactions of methane monooxygenase from *Methylococcus capsulatus* (Bath). *J Am Chem Soc 117*:10174–10185.

Liu KE, Wang D, Huynh BH, Edmondson DE, Salifoglou A, Lippard SJ. 1994. Spectroscopic detection of intermediates in the reaction of dioxygen with the reduced methane monooxygenase hydroxylase from *Methylococcus capsulatus* (Bath). *J Am Chem Soc 116*:7465–7466.

Liu Y, Nesheim JC, Lee SK, Lipscomb JD. 1995c. Gating effects of component B on oxygen activation by the methane monooxygenase hydroxylase component. *J Biol Chem 270*:24662–24665.

Martinis SM, Atkins WM, Stayton PS, Sligar SG. 1989. A conserved residue of cytochrome P-450 is involved in heme-oxygen stability and activation. *J Am Chem Soc 111*:9252–9253.

McMurry TJ, Groves JT. 1986. Metalloporphyrin models for cytochrome P-450. In: Ortiz de Montellano PR, ed. *Cytochrome P-450 structure, mechanism, and biochemistry*. New York: Plenum. pp 1–28.

Nesheim JC, Lipscomb JD. 1996. Large isotope effects in methane oxidation catalyzed by methane monooxygenase: Evidence for C-H bond cleavage in a reaction cycle intermediate. *Biochemistry 35*:10240–10247.

Nicholls A, Sharp KA, Honig B. 1991. Protein folding and association: Insights from the interfacial and thermodynamic properties of hydrocarbons. *Proteins Struct Funct Genet 11*:281–296.

Nordlund P, Dalton H, Eklund H. 1992. The active site structure of methane monooxygenase is closely related to the binuclear iron center of ribonucleotide reductase. *FEBS Lett 307*:257–262.

Nordlund P, Sjöberg BM, Eklund H. 1990. Three-dimensional structure of the free radical protein of ribonucleotide reductase. *Nature 345*:593–598.

Ohlendorf DH. 1994. Accuracy of refined protein structures. II. Comparison of four independently refined models of human interleukin 1β. *Acta Crystallogr D 50*:808–812.

Ortiz de Montellano PR. 1986. Oxygen activation and transfer. In: Ortiz de Montellano PR, ed. *Cytochrome P-450 structure, mechanism, and biochemistry*. New York: Plenum Press. pp 217–271.

Otwinowski Z. 1993. *An oscillation data processing suite for macromolecular crystallography*. New Haven, Connecticut: Yale University.

Patel RN, Savas JC. 1987. Purification and properties of the hydroxylase component of methane monooxygenase. *J Bacteriol 169*:2313–2317.

Paulsen KE, Liu Y, Fox BG, Lipscomb JD, Münck E, Stankovich MT. 1994. Oxidation–reduction potentials of the methane monooxygenase hydroxylase component from *Methylosinus tricosporium* OB3b. *Biochemistry 33*:713–722.

Pilkington SJ, Dalton H. 1990. Soluble methane monooxygenase from *Methylococcus capsulatus* Bath. *Methods Enzymol 188*:181–190.

Poulos TL, Finzel BC, Gunsalus IC, Wagner GC, Kraut J. 1985. The 2.6-Å crystal structure of *Pseudomonas putida* cytochrome P-450*. *J Biol Chem 260*:16122–16130.

Priestley ND, Floss HG, Froland WA, Lipscomb JD, Williams PG, Morimoto H. 1992. Cryptic stereospecificity of methane monooxygenase. *J Am Chem Soc 114*:7561–7562.

Que L Jr, Dong Y. 1996. Modeling the oxygen activation chemistry of methane monooxygenase and ribonucleotide reductase. *Acc Chem Res 29*:190–196.

Rataj MJ, Kauth JE, Donnelly MI. 1991. Oxidation of deuterated compounds by high specific activity methane monooxygenase from *Methylosinus trichosporium*: Mechanistic implications. *J Biol Chem 266*:18684–18690.

Rosenzweig AC, Frederick CA, Lippard SJ. 1992. Crystallization and preliminary X-ray analysis of the methane monooxygenase hydroxylase protein from *Methylococcus capsulatus* (Bath). *J Mol Biol 227*:583–585.

Rosenzweig AC, Frederick CA, Lippard SJ, Nordlund P. 1993. Crystal structure of a bacterial non-haem iron hydroxylase that catalyses the biological oxidation of methane. *Nature 366*:537–543.

Rosenzweig AC, Nordlund P, Takahara PM, Frederick CA, Lippard SJ. 1995. Geometry of the methane monooxygenase catalytic diiron center in two oxidation states. *Chem & Biol 2*:409–418.

Shu L, Liu Y, Lipscomb JD, Que L Jr. 1996a. EXAFS studies of the methane monooxygenase hydroxylase component from *Methylosinus trichosporium* OB3b. *J Biol Inorg Chem 1*:297–304.

Shu L, Nesheim JC, Kauffmann K, Münck E, Lipscomb JD, Que L Jr. 1996b. An $Fe^{IV}{}_2O_2$ diamond core structure for the key intermediate Q of the methane monooxygenase. *Science 275*:515–518.

Stainthorpe AC, Lees V, Salmond GP, Dalton H, Murrell JC. 1990. The methane monooxygenase gene cluster of *Methylococcus capsulatus* (Bath). *Gene 91*:27–34.

Stainthorpe AC, Murrell JC, Salmond GP, Dalton H, Lees V. 1989. Molecular analysis of methane monooxygenase from *Methylococcus capsulatus* (Bath). *Arch Microbiol 152*:154–159.

Sturgeon BE, Burdi D, Chen S, Huynh BH, Edmondson DE, Stubbe J, Hoffman BM. 1996. Reconsideration of X, the diiron intermediate formed during cofactor assembly in *E. coli* ribonucleotide reductase. *J Am Chem Soc 118*:7551–7557.

Thich JA, Ou CC, Powers D, Vasiliou B, Mastropaolo D, Potenza JA, Schugar HJ. 1976. Molecular structure and magnetic properties of μ-dihydroxo-bis[2,6-pyridinedicarboxylatoaquoiron(III)] and μ-dihydroxo-bis[4-hydroxo-2,6-pyridinedicarboxylato-aquoiron(III)] tetrahydrate. *J Am Chem Soc 98*:1425–1433.

Thomann H, Bernardo M, McCormick JM, Pulver S, Andersson KK, Lipscomb JD, Solomon EI. 1993. Pulsed EPR studies of mixed valence [Fe(II)Fe(III)] forms of hemerythrin and methane monooxygenase: Evidence for a hydroxide bridge. *J Am Chem Soc 115*:8881–8882.

Tsien HC, Brusseau GA, Hanson RS, Wackett LP. 1989. Biodegradation of trichloroethylene by *Methylosinus trichosporium* OB3b. *Appl Environ Microbiol 55*:3155–3161.

Wallar BJ, Lipscomb JD. 1996. Dioxygen activation by enzymes containing binuclear non-heme iron clusters. *Chem Rev 96(7)*:2625–2657.

Woodland MP, Dalton H. 1984. Purification and characterization of component A of the methane monooxygenase from *Methylococcus capsulatus* Bath. *J Biol Chem 259*:53–59.

Zang Y, Pan G, Que L Jr, Fox BG, Münck E. 1994. First diferric complex with an $Fe_2(\mu\text{-O})$ (μ-OH) core. Structure and reactivity of $[Fe_2(\mu\text{-O})$ (μ-OH) $(6TLA)_2](ClO_4)_3$. *J Am Chem Soc 116*:3653–3654.